JOURNAL OF PROPULSION AND POWER
Vol. 23, No. 4, July–August 2007

Modeling of the Pulsed Inductive Thruster Operating with Ammonia Propellant

Pavlos G. Mikellides* and Nalin Ratnayake†
Arizona State University, Tempe, Arizona 85287-6106

DOI: 10.2514/1.26609

Comparisons of numerical simulations to experimental data are used to validate the code and offer insights into the highest-to-date performance of ammonia propellant compared to other tested propellants. The time-dependent, two-dimensional, axisymmetric magnetohydrodynamics code used for the simulations is upgraded by a new two-temperature thermochemical model that provides ammonia's thermodynamic properties including nitrogen ionization up to the fifth level. The comparisons to experimental data include magnetic field waveforms at two locations and total impulse values for a range of operating energy levels and propellant mass values. The relatively good agreement of the code's predictions and experiment allows further interrogation of the pertinent plasma flow characteristics and offers a possible explanation as to the elevated efficiency demonstrated by the thruster operated with ammonia propellant.

Nomenclature

B	=	magnetic field
C	=	capacitance
E	=	energy
I	=	total impulse
J	=	current
L	=	inductance
$\dot{L}$	=	inductance rate
M	=	atomic mass
m	=	propellant mass
n	=	number of electrons
Q	=	ionization energy
R	=	resistance
Rm	=	magnetic Reynolds number
r, θ, z	=	cylindrical dimensions
t	=	time
U_e	=	effective exhaust velocity
V	=	voltage
v	=	velocity
Z	=	impedance
ζ	=	average charge state
η	=	plasma electrical resistivity
$\tilde{\eta} = \eta/\mu_o$	=	magnetic diffusivity
η_e	=	efficiency
μ_o	=	$4\pi \times 10^{-7}$ H/m

Subscripts

e	=	electron or external
H	=	heavy particle
o	=	stored or initial
p	=	plasma

Presented as Paper ICOPS-2006-2A4, International Conference on Plasma Science, Traverse City, MI, 4–8 June 2006; received 17 July 2006; revision received 4 February 2007; accepted for publication 4 February 2007.

*Assistant Professor, Department of Mechanical and Aerospace Engineering, P.O. Box 876106; Pavlos.Mikellides@asu.edu. Member AIAA.

†Undergraduate Research Assistant, Honors Program, Department of Mechanical and Aerospace Engineering, P.O. Box 876106. Member AIAA.

Introduction

THE pulsed inductive thruster (PIT) is an electromagnetic propulsion system with potential advantages over other high power electric rockets due to a combination of its distinctive physical operation and demonstrated performance [1]. A spiral induction coil, which is powered by a series of capacitors in Marx-loop configurations, produces a strong azimuthal electric field as the pulsed current passes through. The field breaks down the slug of propellant injected over the surface of the flat coil from the forward pylon and the associated radial magnetic field induces an azimuthal current within a thin gas layer (Fig. 1). This current interacts with the magnetic field to produce an axially directed electromagnetic force. Such inductive acceleration circumvents the need for electrodes and the erosion-related lifetime limitations that have plagued traditional electromagnetic thrusters, even though some coil and pylon erosion may be possible. The PIT has been operated in single-shot discharge mode with a large range of propellants, but demonstrated its highest performance when using ammonia fuel. Specifically, the PIT-MkV when operated with ammonia at a pulse energy of 4.6 kJ demonstrated nearly constant efficiencies exceeding 50% for a wide range of specific impulse values, I_{sp}; 4000 s $< I_{sp} <$ 8000 s [1], with an impulse range I from 0.05 to 0.15 N · s. The pulsed repetition can be tailored to take advantage of available in-space power, and the thruster is well suited for space missions such as on-orbit maneuvering, lunar and Mars cargo delivery, and robotic exploration of the solar system.

Recently, the magnetohydrodynamics (MHD) code, MACH2 [2] (multiblock arbitrary coordinate hydromagnetic), modeled PIT performance over operating energies of 900–1764 J for a wide range of helium and argon propellant mass values [3]. The computed effective exhaust speed $U_e = I/m$ as a function of specific operating energy $e_o = E_o/m$ compared favorably to the experimental data as shown in Figs. 2 and 3.

The analysis showed that helium, argon, and carbon dioxide all operated at approximately 0.2 thrust efficiency, $\eta_e = U_e^2/2e_o$, in the range of 900–1764 J regardless of operating conditions. The MACH2 modeling confirmed the experimental observation by calculating an energy budget that demonstrated the sum of all energy sinks other than kinetic energy was independent of operating conditions. An idealized model extended the confirmation to carbon dioxide as well [2]. However, ammonia operated at approximately 0.22–0.31 thrust efficiency (see Fig. 16, $\eta_e = U_e^2/2e_o$) for the same energy-level range, 900–1764 J. Furthermore, the energy budget from the numerical simulations captured the "critical-mass" phenomenon observed by experiments. This phenomenon is identified by a decrease in efficiency upon operation below a critical propellant mass value. This was extended by the idealized model to a

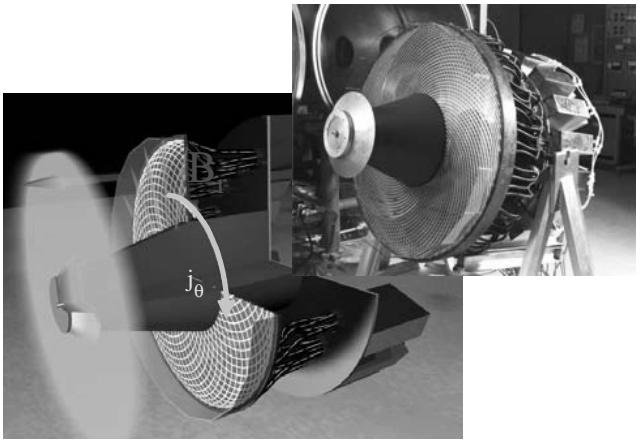

Fig. 1 The pulsed inductive thruster (PIT) and a schematic of the main acceleration process due to the interaction of the applied radial field and the induced azimuthal current. (Courtesy of NGC).

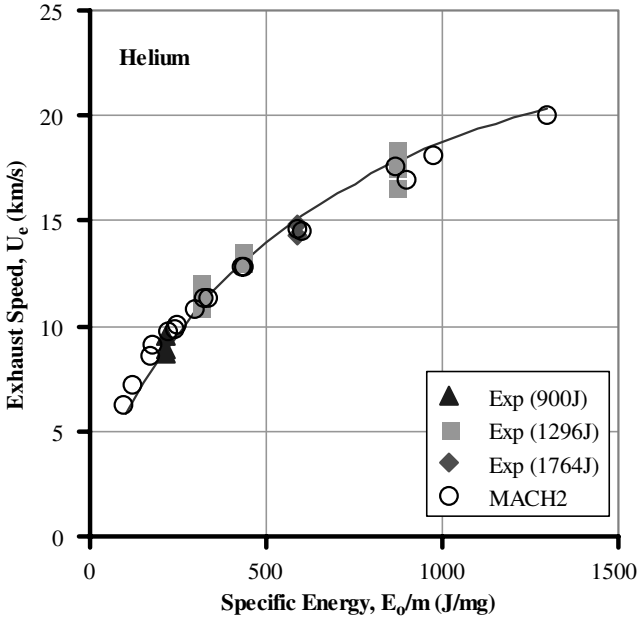

Fig. 2 Comparisons of MACH2 predicted effective exhaust velocity to experimental data for helium propellant.

"critical specific energy, e_o^*" which can be used to predict this critical propellant mass value and guide experimental operation for any propellant type.

The objectives of the effort presented in this paper are to present supporting evidence of the PIT's performance operating with ammonia propellant by exercising MACH2 updated with a new thermodynamic model for ammonia and compare computational predictions to experimental data. Furthermore, the modeling results are used to propose insights in deciphering ammonia's elevated performance over a wide range of other fuels which included helium, argon, carbon dioxide, and hydrazine. As previously mentioned none of these propellants produced commensurate efficiency values to ammonia when operated at the same conditions [1].

Numerical Model

MACH2 is a time-dependent, two-dimensional, axisymmetric, multimaterial code that can be applied to problems of complex geometries [4] due to its multiblock structure. The mesh can be refined via a variety of adaptive schemes to capture regions of varying characteristic scale. The set of the single-fluid, MHD equations is time advanced with finite-volume spatial differencing,

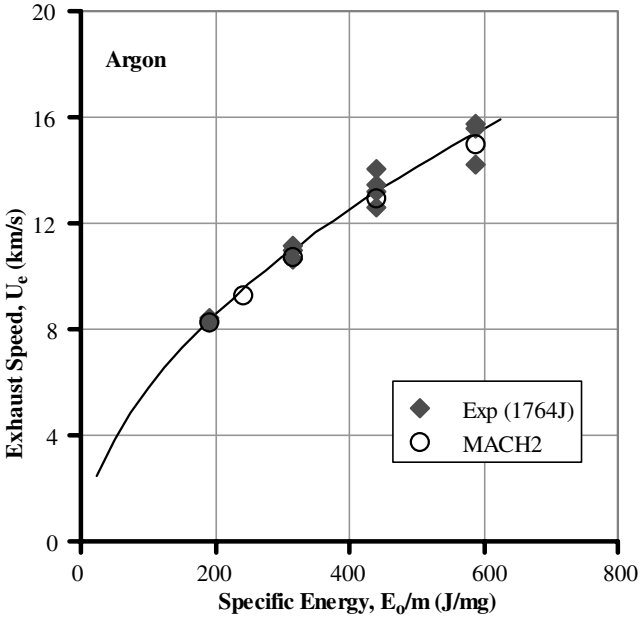

Fig. 3 Comparisons of MACH2 predicted effective exhaust velocity to experimental data for argon propellant.

and the boundary conditions are applied via the ghost-cell technique so that no special conditional statement is necessary at the boundaries.

The mass continuity and momentum equations assume a compressible, viscous fluid with the latter including both real and artificial viscosity effects. The electrons and ions are in thermal nonequilibrium, so MACH2 solved two energy equations for this effort. These include classical thermal conduction with optically thin Planck radiation. Evolution of the magnetic field is prescribed by the induction equation that includes resistive diffusion with various models for the plasma resistivity. The modeling used classical resistivity [5], including contributions from electron-neutral collisions applicable to weakly ionized gases [6]. In many engineering applications the source of magnetic flux is applied currents produced from externally applied voltage differentials. For this, the code includes a variety of circuit models, the pertinent one used in the simulations is an inductance–resistance–capacitance (LRC) model. The set of the MHD equations is completed by functional relationships for the equations of state that can be either analytic or tabular. The SESAME library [7] is the tabular model used for the simulations that includes semi-empirical models for the thermodynamic properties, transport coefficients (including opacities), and average ionization states under local thermodynamic equilibrium (LTE). The SESAME tables were used for the He/Ar simulations; however, the existing SESAME thermodynamic model for ammonia was inadequate for the high-temperature, low-pressure PIT operation, so a new thermal nonequilibrium ($T_e \neq T_H$) LTE model was developed and converted to the proper tabular SESAME form for the ammonia simulations [8]. Briefly, the new LTE NH_3 thermochemical model includes dissociation and ionization reactions up to five ionization levels for nitrogen and provides the thermodynamic properties for a range of the two independent state variables of $10^{-7} < \rho < 1$ kg/m^3 and 300 K $< T_{e,H} <$ 50 eV.

Pulsed Inductive Thruster Physical Modeling

A substantial body of experimental data is available for the PIT comprising a diverse range of propellants, energy levels, and propellant mass values [1]. The thruster power supply consists of a series of 18 capacitors in Marx-loop pairs that are charged in parallel. This results in an effective discharge voltage that is double that of each capacitor's charge voltage which in turn provides the necessary high electric field for breakdown. In particular, the configuration results in an effective capacitance and voltage that relate to the single

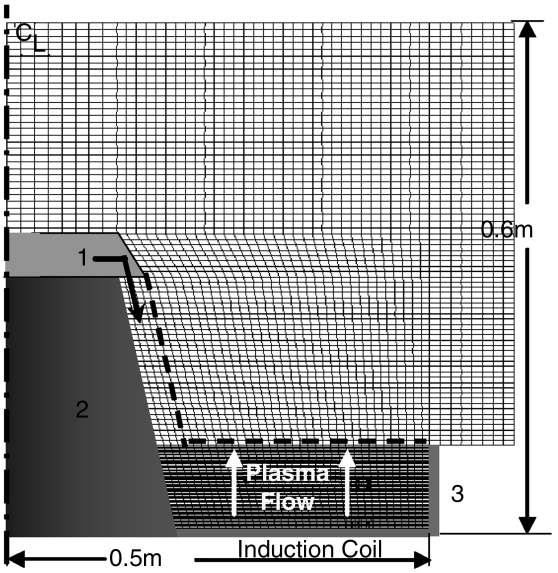

Fig. 4 Schematic of the half-plane thruster with the computational grid used (not to scale). 1: Nozzle with pulsed mass valve showing propellant mass injection; 2: conical pylon; 3: confining cuff (Lexan^{TM}) extending 10 cm downstream of the coil.

capacitance and charge voltage through the total energy available:

$$E_o = \tfrac{1}{2}(\text{no. of capacitors})CV_o^2 = \tfrac{1}{2}C_{\text{eff}}V_{\text{eff}}^2 \qquad (1)$$

where $V_o = 1/2V_{\text{eff}}$. For the high-energy ($E_o > 2304$ J) polyatomic propellant experiments the effective capacitance was 9 μF, whereas the earlier efforts with monatomic and polyatomic propellants at lower energy levels ($900 < E_o < 2304$ J) used smaller capacitors with effective capacitance of 4.5 μF [1]. The slug of propellant mass is introduced through a nozzle (Fig. 4) by a fast opening gas valve. For optimal distribution of the injected gas the mass pulse is short enough that it ceases as the leading edge reaches the confining Lexan^{TM}. In operation, the propellant slug is injected and a time delay is used to time the capacitor discharge at the optimal propellant distribution. The resulting oscillatory current waveform provided a pulse duration of the order of 15 μs with peak currents exceeding 100 kA for charging voltages between $10 < V_o < 16$ kV and propellant mass values of $1.5 < m < 10$ mg.

The thruster's performance data exhibited approximately constant-efficiency trends for a wide range of specific impulse values ($500 < I_{\text{sp}} < 9000$ s) providing impulses exceeding 0.1 N · s at the higher energy levels.

The first set of MACH2 simulations described below uses the new ammonia equation of state for comparisons to experimental impulse and magnetic field waveforms for one high-energy case, namely, operation at 4050 J of stored energy and 4.3 mg of injected propellant mass. The main modeling effort follows, addressing simulations of the lower energy regime ($900 < E_o < 2304$ J), for a range of propellant mass values. The MACH2 model includes thermal nonequilibrium of a single fluid with classical transport. Boundary conditions are modeled as thermal and magnetic field insulators with no slip. The computational grid (Fig. 4) extends well downstream of the thruster's exhaust region to fully capture the acceleration process and assure no influence of the zero-gradient outlet boundary conditions. The grid resolution is maximized in the vicinity of the coil to assure capture of the fast-rising field's diffusion and associated gradient.

Initial conditions assigned uniform gas density in the vicinity of the coil and along the column extending upstream of the injection nozzle (the confined region identified by the dotted line in Fig. 4) to represent the evolved gas injected from the valve. The initial, uniform gas temperature is set to 300 K. The potential significance of nonuniformities due to the gas injection scheme was addressed by a separate series of simulations, which showed negligible differences when compared to the simplified initial conditions outlined previously [9]. Specifically, those simulations modeled the actual expanding flow from the nozzle to the induction coil according to the experimental procedure and the discharge was initiated once the flow arrived at the confining Lexan^{TM}. These initial conditions assure that ionization of the gas occurring after the breakdown is self-consistently calculated by the MACH2 ionization model along with the evolution of the rest of the pertinent variables as opposed to simply assuming an initial ionization state. The resistivity model includes contributions from electron–ion Coulomb collisions and electron-neutral collisions [2].

PIT Modeling Operating at $E_o = 4050$ J and $m = 4.3$ mg

PIT operation with NH_3 at 4050 J and 4.3 mg is the only case for which experimental magnetic probe measurements were performed and thus provides the opportunity for useful comparisons to details of the flow as opposed to impulse comparisons that represent an integrated quantity. Emulation of the current waveform used the LRC circuit model in MACH2 and was partially guided by the experimental waveforms which are shown in Fig. 5 for two different axial locations and a radial location of 40 cm. The axial location identified by $z = 0.5$ cm represents placement of the magnetic probe at the induction coil and is indicative of the evolution of the circuit waveform [1] via $J(t) = (r_o - r_i)B_r(t)/\mu_o$. Because no experimental current waveforms were available, the magnetic field waveform of Fig. 5 was used to set the only two independent variables of the MACH2 LRC circuit, namely, external resistance and inductance. These were computed so as to capture peak current and rise times at the induction coil, $z = 0$. There are two important features to note regarding the current waveform modeling: 1) The code's circuit model upgrade that couples the circuit to the plasma is not yet completed, so these simulations do not account for plasma resistance and inductance and rate of change of inductance when the current is computed by the LRC model. 2) The MACH2 magnetic field boundary condition is the sole mechanism that introduces magnetic energy to the plasma by setting the ghost-cell value to $B_r(t) = \mu_o J(t)/(r_o - r_i)$, thus allowing magnetic field evolution in response to the plasma dynamics at $z = 0$. The current waveform computed by the LRC circuit for this case, depicted in Fig. 6, is expected to underestimate the second half-period of the waveform, that is, the reversal time and magnitude of the second peak because it does not incorporate the plasma's impedance which will tend to further dampen the sinusoid. Comparisons of the computed magnetic field at the two different axial locations are represented by Figs. 7 and 8 wherein the experimental waveforms have been reproduced for clarity. At the induction coil location we note the expected capture of peak field value and rise time and the underestimation of the second peak and reversal time. The discrepancy between the first reversal times can also be used as a quantitative assessment of the relative coupling between plasma and magnetic field. Specifically, the delay

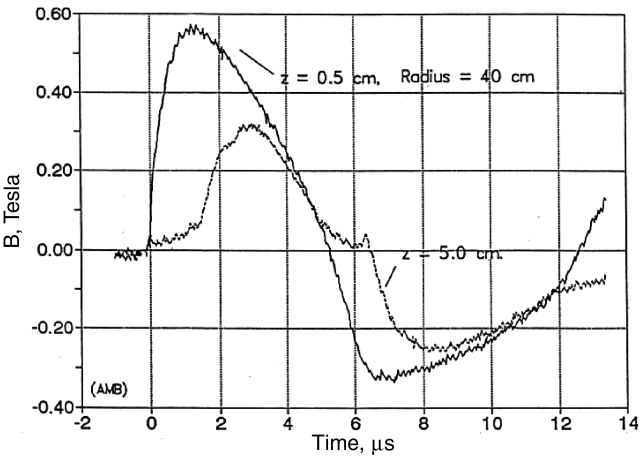

Fig. 5 Experimental magnetic field waveforms obtained with 4.3 mg of NH_3 propellant and 4050 J of stored energy.

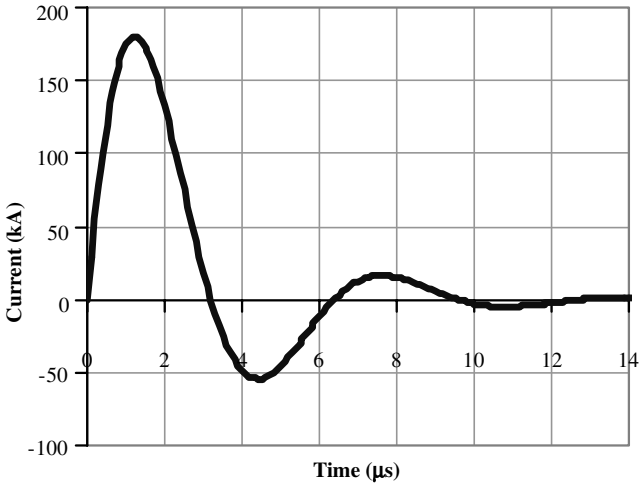

Fig. 6 Coil current waveform used by MACH2 to model operation at 4050 J with 4.3 mg of NH_3 propellant.

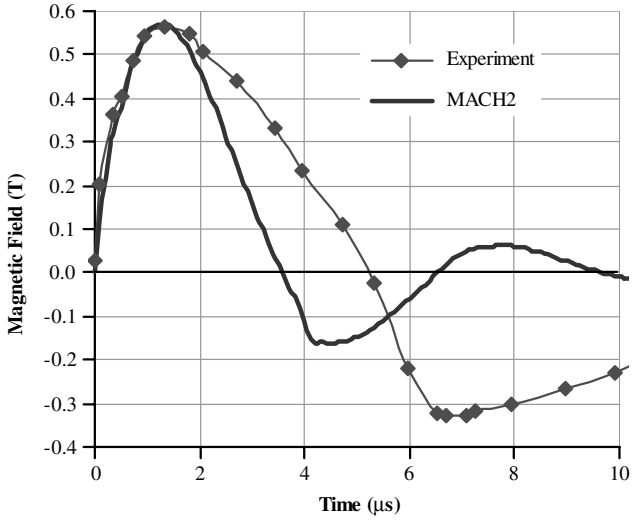

Fig. 7 Magnetic field waveform comparison at the induction coil ($z = 0$) and radial location of 40 cm.

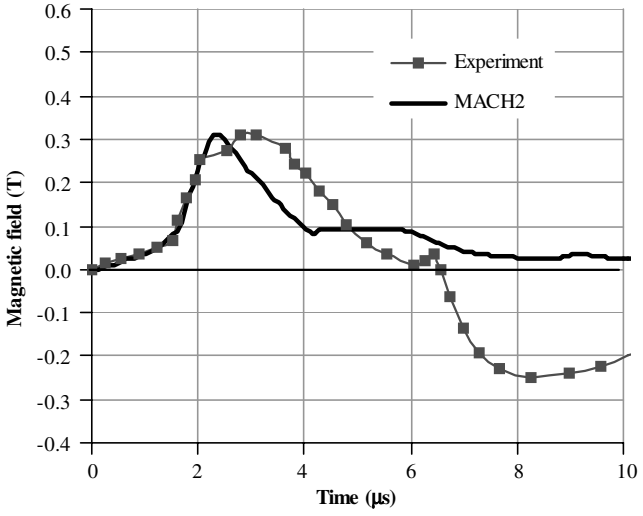

Fig. 8 Magnetic field waveform comparison at an axial location of 5 cm downstream of the induction coil and radial location of 40 cm.

in field reversal, that is, the asymmetry of the field waveform, indicates an elevated plasma impedance which if dominated by the rate of change of inductance as opposed to plasma resistance indicates elevated work done by the electromagnetic force on the plasma, thus elevated kinetic energy conversion. This is, in other words, an indication of an elevated inductance change which is associated with efficient acceleration. The more relevant comparison with respect to the capability of the computations in capturing the pertinent acceleration mechanisms is the field waveform comparison at the downstream location of 5 cm (Fig. 8). The predicted field captures both rise time and magnitude indicating that the code properly computes arrival time and current conduction zone thickness. This is very encouraging as it implies that the code includes the appropriate models to prescribe the field-plasma coupling in terms of dynamics and resistive diffusion and thus allows further interrogation of the pertinent plasma properties that can lead to improved understanding. Before we proceed to characterize flow properties it is of interest to note the relative delay, in this case more pronounced than the waveform at the induction coil, in the field reversals shown in Figs. 7 and 8. Qualitatively the code captures these features, but the magnitudes and periods differ due to exclusion of circuit response to plasma dynamics. Based on the quantitative agreement between simulation and experiment for the first half-period of the waveform we proceed to compare predicted impulse to experimental measurements.

Thrust was calculated as the integral of the total pressure at the outlet boundary and integrated over time to provide the impulse. Although the effective pulse duration was about 14 μs computational times were in excess of 100 μs so as to capture all the propellant exhausted through the downstream boundaries. The calculated thrust histogram for the 4050 J, 4.3 mg case is shown in Fig. 9. The sharp rise of the thrust value at about 16 μs suggests exhaust of a compact plasma at 37.5 km/s consistent with a slug-acceleration motion. The reduced gradient after the first peak suggests a more dispersed plasma that takes longer to pass through the downstream boundary. The width of the pulse also indicates the degree of effective coupling and the eventual exhaust speed: a narrower histogram with higher peak thrust values indicates better coupling and thus increased exhaust velocities for the same propellant mass and energy level. A second thrust maximum at about 1/4 of the value of the first maximum is identified at 47 μs (corresponding to speeds of around 12.8 km/s) and demonstrates additional electromagnetic acceleration from the second half-period of the current waveform. Because of the underestimation of the second maximum magnetic field value (Fig. 5) this second peak is also underestimated which eventually leads to the 10% discrepancy

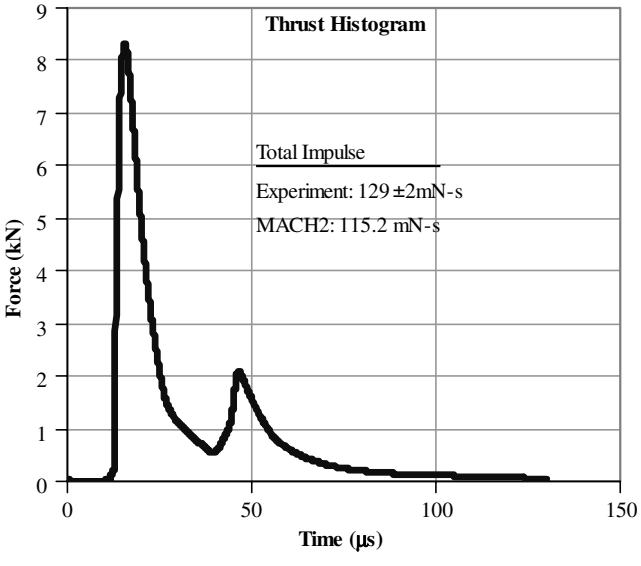

Fig. 9 Calculated thrust as a function of time and impulse comparison for 4050 J and 4.3 mg.

between the total measured and computed impulse (see the legend of Fig. 9 for the experimental comparison). Assuming that thrust scales with magnetic pressure, then the higher experimental magnetic field displayed by Fig. 7 leads to an additional maximum thrust increase of about 23% over the computed value. However because the main acceleration occurs during the first half-cycle, which is adequately captured by MACH2, it is thus useful to interrogate the calculated plasma properties to obtain further insights into the acceleration mechanisms. Figures 10–14 display the two-dimensional distributions of the mass density and axial profiles of the magnetic pressure and mass density at a radial location of 40 cm for different times. Each figure caption also includes calculated values for electron T_e

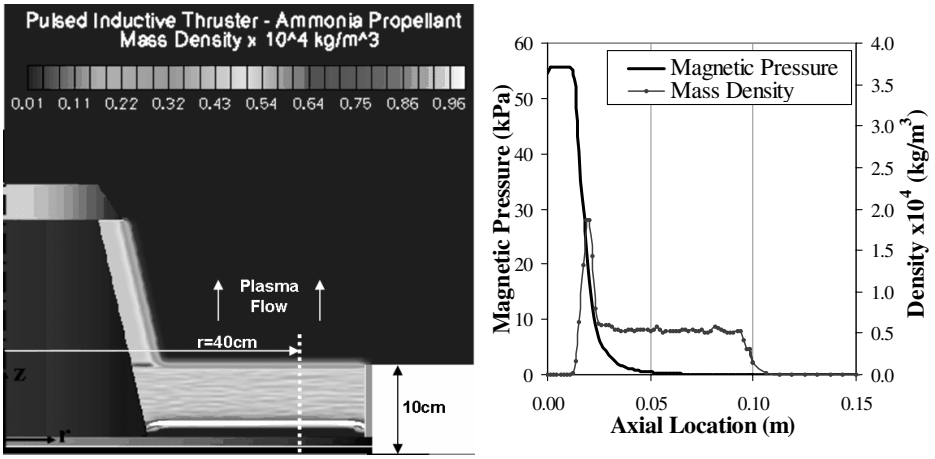

Fig. 10 Time = 1 μs. Left: Computed two-dimensional mass-density distribution. Right: Axial (z) distributions of magnetic pressure and mass density at a radial location of 40 cm. At maximum density, $\rho = 0.187$ gm/m^3: $T_e = 2.44$ eV, $T_H = 2.41$ eV, $\zeta = 1.17$, and $v_z = 25.12$ km/s.

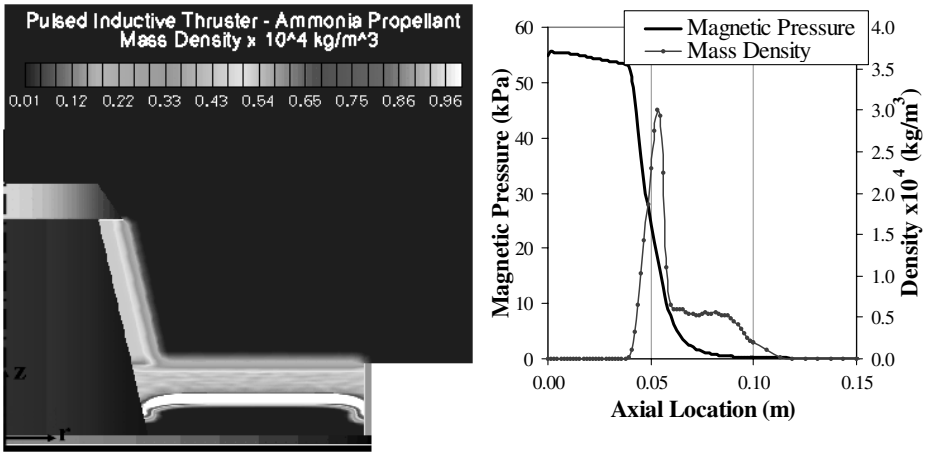

Fig. 11 Time = 2 μs. Left: Computed two-dimensional mass-density distribution. Right: Axial (z) distributions of magnetic pressure and mass density at a radial location of 40 cm. At maximum density, $\rho = 0.3$ gm/m^3: $T_e = 2.72$ eV, $T_H = 2.71$ eV, $\zeta = 1.2$, and $v_z = 30.42$ km/s.

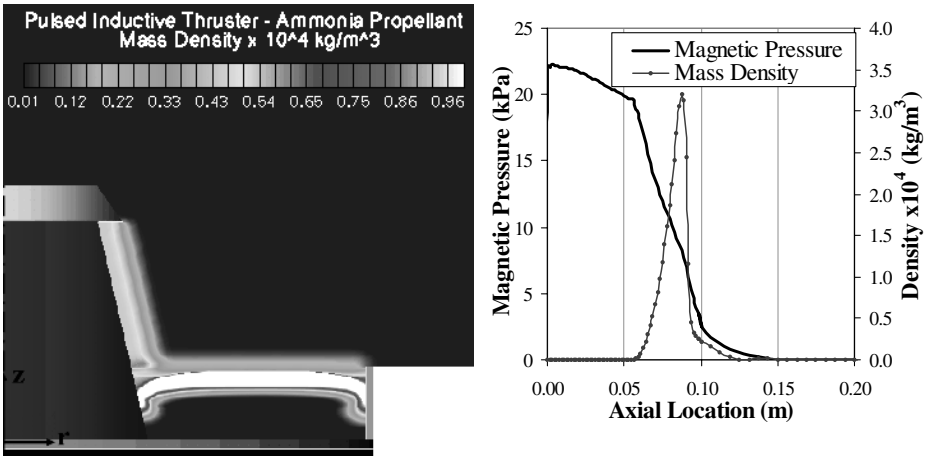

Fig. 12 Time = 3 μs. Left: Computed two-dimensional mass-density distribution. Right: Axial (z) distributions of magnetic pressure and mass density at a radial location of 40 cm. (The abscissa is extended to 20 cm.) At maximum density, $\rho = 0.321$ gm/m^3: $T_e = 2.37$ eV, $T_H = 2.37$ eV, $\zeta = 1.11$, and $v_z = 27.89$ km/s.

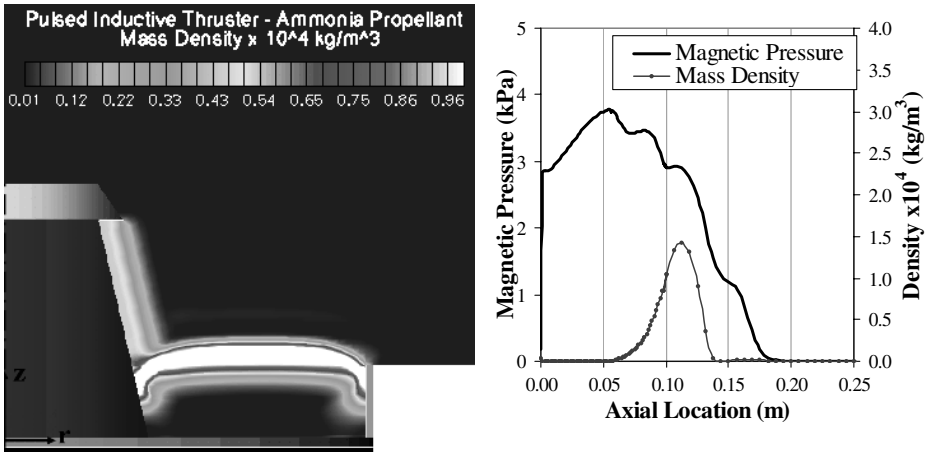

Fig. 13 Time = 4 μs. Left: Computed two-dimensional mass-density distribution. Right: Axial (z) distributions of magnetic pressure and mass density at a radial location of 40 cm. (The abscissa is extended to 25 cm.) At maximum density, $\rho = 0.142$ gm/m^3: $T_e = 2.1$ eV, $T_H = 2.1$ eV, $\zeta = 1.06$, and $v_z = 27.68$ km/s.

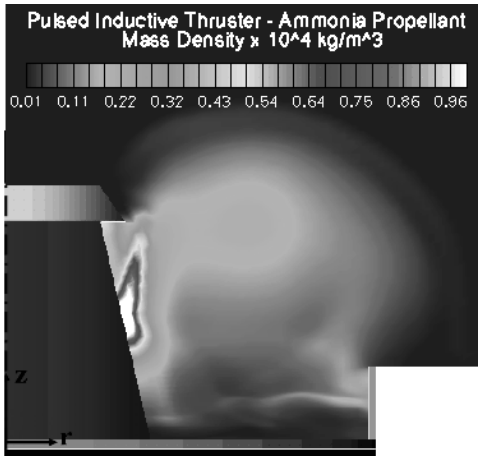

Fig. 14 Computed two-dimensional mass-density distribution at 10 μs.

and heavy particle T_H temperature and average charge $\zeta = n_e/n_H$ at maximum density. Examination of the relevant distributions at 1 μs identifies a relatively efficient accelerator. Primarily, we note that the two-dimensional mass-density distribution shows an approximately uniform plasma distribution over the radius—except for some variation near the solid walls—which in turn implies that the axial distributions (at $r = 40$ cm) are approximately representative of the entire propellant. It is important to note that the density scale for all two-dimensional distributions presented is limited to a maximum of 10^{-4} kg/m^3 even though maximum density values exceed 3×10^{-4} kg/m^3. This was necessary to improve clarity but most importantly to show evolution of the thickness of the current conduction zone at the expense of additional resolution within the layer.

The axial distributions depict only a portion of the gas coupled to the magnetic field and thus participating in the electromagnetic acceleration. This is evident from the extent of the magnetic field gradient. The rest of the propellant is relatively cold and mostly consists of neutral gas which provides energy sinks such as heating and ionization. The neutral gas is entrained by the accelerating plasma in an anticipated snowplow fashion. If we assume that the effective current conduction zone z_o extends to 0.05 of the peak magnetic pressure value then the axial profile at 1 μs yields $z_o = 2.35$ cm. Calculating representative values at peak mass density yields an effective speed of $v_{\text{eff}} = 25.1$ km/s and a magnetic diffusivity $\tilde{\eta} = \eta/\mu_o = 142$ m^2/s. Using these values we can calculate and compare inductance rate $\dot{L}$ to the effective plasma resistance R_p:

$$\dot{L} = \frac{\pi\mu_o(r_o + r_i)}{(r_o - r_i)} v_{\text{eff}} = 230.3 \text{ m}\Omega > R_p$$
$$= \frac{\pi\mu_o(r_o + r_i)}{(r_o - r_i)} \frac{\tilde{\eta}}{z_o} = 55.6 \text{ m}\Omega \quad (2)$$

or more conveniently the ratio,

$$\frac{\dot{L}}{R_p} = \frac{v_{\text{eff}} z_o}{\tilde{\eta}} = 4.14 > 1$$

This is indicative of efficient acceleration as it shows that the work done on the plasma sheet by the electromagnetic force dominates deposition of energy via joule heating. The ratio is of course the magnetic Reynolds number Rm, which shows that field convection dominates over diffusion, that is, the necessary induced azimuthal currents are substantial. Including external resistance losses in the circuit's fixed elements does not change the general conclusion as the external resistance was experimentally inferred to be 5 mΩ [1]. Thus, at best the efficiency (work done by the accelerating plasma to the total energy deposited to the plasma) η_e scales as $\eta_e \sim 1/2\dot{L}/(R_p + 1/2\dot{L}) = Rm/(2 + Rm)$. At peak density the plasma electron temperature is calculated to be 2.44 eV with an average charge $\zeta = 1.17$. The latter implies a fully ionized mixture of nitrogen and hydrogen ions with the nitrogen ions slightly doubly ionized. Note that $\zeta = n_e/n_H = 1$ denotes four free electrons per four heavy particles which represent the three hydrogen ions and one nitrogen ion. Thus, in this case the nitrogen ion is singly ionized if we assume that all hydrogen atoms are fully ionized. $\zeta = 2$ represents two electrons per heavy particle or a total of eight electrons per ammonia molecule, or fully ionized hydrogen and fully fifthly ionized nitrogen.

The distributions at 2 μs (Fig. 11) continue to depict an approximately radially uniform plasma acceleration with a persisting efficient coupling denoted by a minimal widening of the current sheet to $z_o = 3.13$ cm. Once again based on MACH2 calculated values of $v_{\text{eff}} = 30.4$ km/s and $\tilde{\eta} = 122$ m^2/s, the relative ratio $\dot{L}/R_p = Rm = 7.78 > 1$ which implies even further improvements in the desired kinetic energy deposition. This is further confirmed by noting that the peak density increases from 0.187 to 0.3 gm/m^3 over approximately the same sheet thickness as more gas is entrained, but the effective electron temperature and average charge have slightly increased to 2.72 eV and 1.2, respectively. If we assume that deposition to translational internal energy (heating) scales as $e = 3/2k(1 + \zeta)T_e$—since $T_H \sim T_e$—and kinetic energy scales as v_{eff} [2], then the translational internal energy has increased by about 13% while the kinetic energy has increased by about 46%. At 3 μs the approximately radial uniformity is maintained even though the majority of the plasma sheet has reached the end of the confining

region. (Even though the scale in the two-dimensional distributions does not include variations above 0.96 gm/m^3 for clarity, the radial uniformity is approximately maintained.) Axial distributions show that the majority of the propellant has by now been entrained by the accelerating sheet and compressed to the highest density. This denotes the end of the "snowplow" phase toward a slug phase characterized by acceleration of the entire propellant mass. They also show that as the magnetic field decreases the field gradient and thus the induced azimuthal current density are decreasing as well and are associated by a broadening of the current conduction zone to approximately $z_o = 5.67$ cm. The calculated axial speed at peak density is 27.9 km/s which denotes some deceleration, thus a decrease in inductance rate. However, the broadening of the current sheet implies diminished resistive losses [see Eq. (2)], so the efficient coupling is still maintained ($\tilde{\eta} = 136$ m^2/s, $Rm = 11.6$). This efficient coupling is further supported by the decrease of the electron temperature and average charge values to 2.37 eV and 1.11, respectively.

Furthermore, the computed effective plasma impedance is $Z(3\ \mu\text{s}) = R_p + \dot{L} = 206.9$ mΩ which is greater than the fixed circuit resistance used by the MACH2 LRC circuit, leading to the delay in reversal time which is not captured by the code. At 4 μs the computed magnetic field has just reversed while the plasma is now expanding beyond the confining region depicted by the decreased density. Even though at this instant the computed results underestimate the experimentally measured time reversal some qualitative statements can be made. MACH2 predicts some decoupling of the flux and plasma because part of the computed field gradient does not advance in phase with the mass density gradient, but more important, a dispersion of the plasma slug depicted by the decreased density gradient upstream of the maximum density location. Because the initial field gradients are computed in front of a portion of the propellant mass this implies that a finite amount of propellant may still be available for further acceleration by the second half-period of the current waveform. Computed two-dimensional distributions and axial profiles at later times show a secondary conduction zone involving a decreased amount of plasma that is accelerated in a similar snowplow fashion. The calculations also show that the plasma continues to accelerate beyond the confining region due to expansion and conversion of enthalpy to kinetic energy. Although simulations at a later time allow only qualitative comparisons, they nevertheless provide useful insight. As shown in Fig. 14 at 10 μs, there is secondary acceleration resulting from the second field increase. The maximum exhaust velocity achieved by the fully exhausted plasma is about 37.5 km/s, calculated by the thrust histogram (Fig. 9). The thrust histogram also confirms this secondary acceleration; however, the amount of mass coupled to the second increase of the field is substantially less than the main uncoupled plasma that has by now expanded beyond the confining region. Thus, the effective plasma impedance is diminished which leads to a lower current minimum (see Fig. 7) than that calculated by the MACH2 circuit, but at the same time it contributes much less to the total impulse. The discrepancy between the total calculated and measured impulse is still of the order of 10%, which once again is a consequence of both the delay in current reversal and the low magnitude of the second current peak. It is thus premature to extend the computations to a wide range of high-energy levels until the circuit model upgrade is completed. However, it is expected that plasma voltage contributions to the current will be even less at lower energy levels where the associated plasma speeds and magnetic field values will be lower. This presents an opportunity to extend validation and insights, and so the next section presents calculations of PIT operation at the lower energy-level range of $900 < E_o < 2304$ J

PIT modeling for $900 < E_o < 2304$ J

Operation at lower energy levels is expected to reduce plasma voltage contributions, $V_p(t) = L_p\dot{J} + (R_p + \dot{L})J$ to the current waveform compared to the higher energy levels. This is due to the experimentally demonstrated reduction in speed and current values when operating at the lower energy levels. For example, the 4050 J/4.3 mg case operated at an effective capacitor voltage $V_o = 30$ kV and $C = 9\ \mu$F producing peak magnetic field, $B_{mx} = 0.57T$, $I = 129$ mN $\cdot$ s, and thus a thrust efficiency $\eta_e = I^2/mCV_o^2$ of about 0.48. Thus, for the sake of order-of-magnitude approximations we can scale the plasma voltage at peak current as $V_p \sim (R_p + \dot{L})J_{mx}$ where $J_{mx} = B_{mx}(r_o - r_i)/\mu_o$. Combining with the efficiency expression $\eta_e \sim 1/2\dot{L}/(R_p|1/2\dot{L})$,

$$V_p \sim \acute{L}\frac{I}{2m}\left(\frac{1+\eta}{2\eta}\right)J_{mx} \tag{3}$$

where

$$\acute{L} = \frac{\pi\mu_o(r_o + r_i)}{(r_o - r_i)}$$

For the 4050 J/4.3 mg case it is of the order of 29 kV which is commensurate to the total charging voltage of 30 kV. Similar approximation of the plasma voltage for lower initial energy, however, shows its diminishing value as compared to the charging voltage. For 2304 J/1.9 mg the thruster was powered by a capacitor bank of $C = 4.5\ \mu$F charged at 30 kV and produced $I = 57$ mN $\cdot$ s, that is, $\eta_e = 0.37$; thus if we assume that magnetic energy scales with stored energy then B_{mx} scales with $\sqrt{E_o}$ and $V_p \sim 24.6$ kV while the 1296 J/3.8 mg case at $V_o = 24$ kV, $I = 49.5$ mN $\cdot$ s and $\eta_e = 0.25$ indicates plasma voltage contributions of the order of 11.5 kV. The argument suggests that the current waveform computed by MACH2 based only on external fixed circuit elements should better approximate the actual waveform as it is less affected by plasma voltage contributions. It is also expected that the computed total impulse will better corroborate experimental data because additional acceleration due to the second current should be substantially more modest than the high-energy operation. The latter is further supported by the thrust histogram computed by MACH2 for the 2304 J/1.9 mg and 1296 J/3.8 mg cases depicted by Fig. 15. It is apparent, especially when compared to the thrust histogram of the 4050 J/4.3 mg case (Fig. 9), that the second thrust maximum that would correspond to additional acceleration from the second current peak is almost nonexistent. The absence of discernible acceleration due to the second current peak was also evident in the calculations with helium and argon for a wide range of propellant masses and low-energy levels [3].

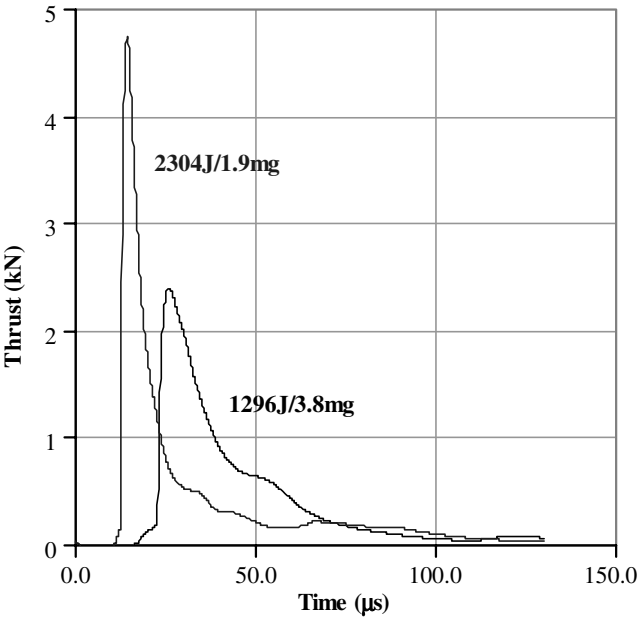

Fig. 15 Computed thrust histogram for two different operating conditions at lower energy levels.

The simulations in the range of 900–2304 J proceeded by using the same circuit model used for the 4050 J/4.3 mg case, thatis, for the same external fixed resistance and inductance values. The LRC model used a capacitance of 4.5 μF according to experiments and varied the charging voltage accordingly. Furthermore, initial and boundary conditions were identical and the computations were performed with the same computational grid presented in Fig. 4. Initial density was adjusted accordingly to correspond to the desired propellant mass. Impulse values were calculated by integrating thrust over a time duration that assured all propellant mass was expelled from the computational region and compared to experimental measurements in Fig. 16. The comparisons are presented in terms of an effective exhaust velocity $U_e = I/m$. The trends and magnitudes are captured relatively well considering the wide range of operating conditions and the deficiency of the LRC circuit coupling which is presumably responsible for the slight underestimation at higher energy levels. The maximum discrepancy, which occurs at the maximum energy level of 2304 J, is about the same as the 4050 J case, that is, 10% as expected from the order-of-magnitude comparisons of the plasma voltage contributions. The overestimation (~3%) for the 900 J/3.8 mg case is addressed later. A significant feature depicted by both experiment and modeling is that efficiency $\eta_e = U_e^2/2e_o$ increases with specific operating energy $e_o = E_o/m$ unlike other propellants which have mainly shown approximately constant efficiency for the same range of operating specific energy (Figs. 1 and 2). In particular, experimental data and modeling showed that He, Ar, and CO_2 operated at approximately constant efficiency of 0.2 for 900–1764 J while NH_3 displays an increase from 0.23 to 0.31 in the same range. The efficiency is further improved at even higher levels reaching 0.37 at 2304 J and eventually the maximum of about 0.48 at 4050 J after doubling the capacitance. In general, one would expect that such electromagnetic devices will display an increasing efficiency with operating energy regardless of propellant choice. This would be a consequence of stronger field-plasma coupling due to elevated temperature values, thus diminished plasma resistivity as well as higher speeds; in other words the Rm increases with increasing energy. However ammonia is the only propellant that displays such behavior. Eventually, NH_3 also exhibited constant efficiency operation at higher energy levels, but this transitional regime identifies the increase toward the eventual 0.50 efficiency that has not been demonstrated by another propellant. Thus, besides the need for an explanation of ammonia's superior efficiency, an additional query arises pertaining to its increasing efficiency with increasing specific energy in this transitional regime of operation.

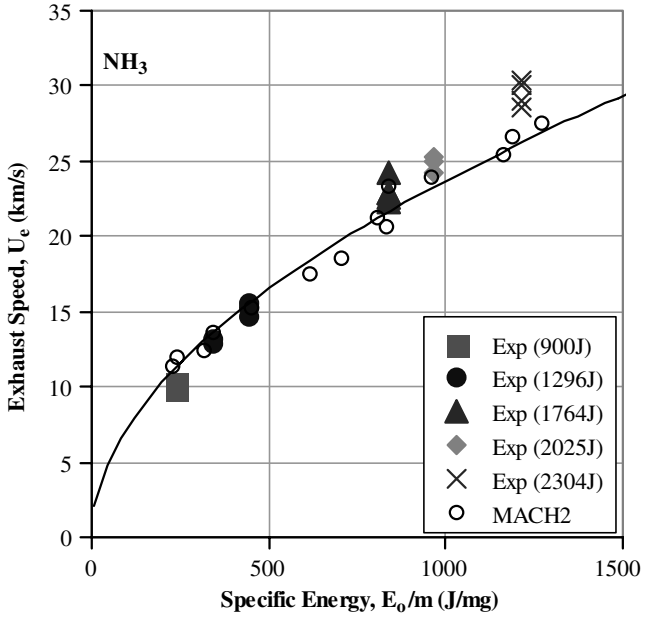

Fig. 16 Comparison of computed effective exhaust velocity $U_e = I/m$ to experimental data as a function of specific operating energy for ammonia propellant.

Explanation of Ammonia's Elevated Performance

Comparisons to experimental data of the MACH2 predictions using fixed resistance and inductance for the current waveform to experimental data have so far concluded the following:

1) The computed magnetic field waveform captures the rise time and magnitude at two different distinct locations, but underestimates reversal time and first field-minimum value at operation with 4050 J of stored energy and 4.3 mg of propellant mass. The critical comparison is the field waveform at the downstream location of 5 cm and radial location of 40 cm because the agreement between modeling and experiment indicates that the highly interacting processes are appropriately modeled by the code. This is because the agreement in both magnitude and arrival time for the magnetic field indicates that the model accurately calculates the field gradient, magnetic energy deposition, and speed of the current sheet. The second peak of the current waveform contributes additional plasma acceleration which leads to underestimation of the impulse computed by 10%.

2) Modeling at lower energy levels allowed more accurate comparisons to experimental impulse data as the contributions from the second current peak are diminished. Such comparisons showed good agreement for a range of 900–2304 J and 1.9–3.8 mg with some expected underestimation at the higher energy operation due to the aforementioned factor.

All of these simulations of PIT operation with ammonia propellant have been performed without including any energy transfer due to radiation, unlike previous simulations with helium and argon propellants that did include models for radiation cooling of an optically thin (Planckian) medium. The relatively good agreement between MACH2 and experiment implies that indeed ammonia's elevated efficiency values over other propellants may be due to negligible radiation losses. Even though the initial motivation for excluding radiation for the ammonia simulations was to examine the necessity of upgrading the new thermodynamic model with appropriate opacity functions of two independent state variables, the agreement between model and experiment supports the conclusion of negligible radiation heat transfer. To further support the argument we note that comparisons of total impulse as calculated by MACH2 either capture or underestimate the experiment as opposed to an expected overestimation if a significant energy sink is omitted. The code only overestimates one data point at 900 J and 3.8 mg which can be attributed to exclusion of radiation losses as one may expect a somewhat elevated volumetric cooling rate at higher density values. A direct calculation of radiation effects with ammonia propellant is unattainable due to the unavailability of appropriate opacity functions. However, to further support the argument such a calculation was performed with helium propellant at the appropriate 4050 J energy level and 4.3 mg of propellant mass. Specifically, two simulations are compared through the thrust histogram depicted in Fig. 17 that quantify the relative effects of radiation on the overall performance of the thruster. We note that the two thrust histograms are substantially different denoting significant differences in the evolution of plasma acceleration which is reflected by the substantially reduced impulse value when radiation heat transfer is included. The width and peak maximum associated with the first thrust maximum show the weaker coupling between plasma and magnetic field when subjected to radiation losses because these would tend to decrease the effective temperature which leads to elevated plasma resistance. It should also be noted that radiation effects tend to diminish additional acceleration from the second current peak (a second thrust maximum is nonexistent in the thrust histogram when radiation effects are included) which is anticipated due to the cooling effects. Additionally, a comparison of the thrust evolution calculated for ammonia (Fig. 9) and helium without inclusion of radiation effects is quite insightful. They show that in the absence of radiation cooling helium and ammonia produce very similar characteristics including thrust maxima, arrival times at the

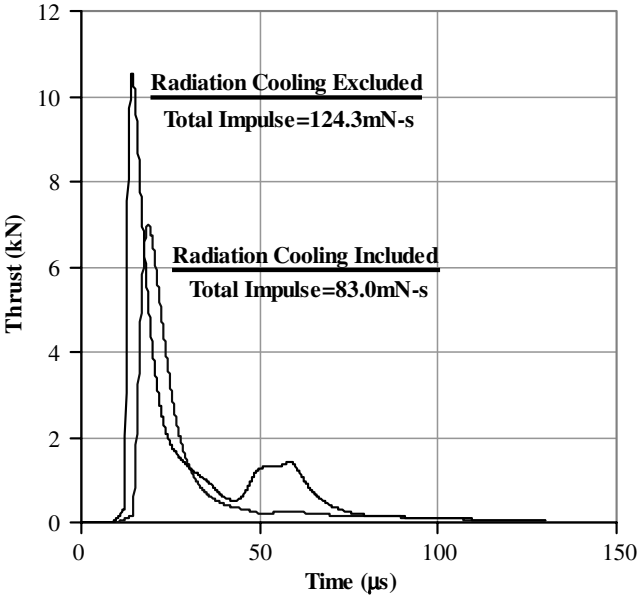

Fig. 17 Calculated thrust histogram of PIT operation with 4.3 mg of helium propellant at 4050 J of stored energy.

same location, and overall performance in terms of total impulse. This supports the argument that if helium was subject to negligible radiation losses it would produce an almost identical performance to ammonia. Equivalently, MACH2 predicts that helium would produce similar efficiency values as that of ammonia, $\eta_{e_{\mathrm{He}}}^{\mathrm{MACH2}} = 0.44$, $\eta_{e_{\mathrm{NH_3}}}^{\mathrm{MACH2}} = 0.38$, and $\eta_{e_{\mathrm{NH_3}}}^{\mathrm{EXP}} = 0.48$, if radiation effects were negligible. The calculations indicate, however, that actual operation with 4.3 mg of helium propellant at 4050 J of stored energy would produce 83 mN · s of impulse, thus the same efficiency value of only 0.2 calculated with helium (see Fig. 2) for a wide range of other operating conditions and consistent with the constant efficiency trend also captured by the calculations. The following order-of-magnitude argument provides further explanation as to the diminished effects of ammonia's radiation losses. Based on Stefan–Boltzmann's law the volumetric cooling rate is

$$P_{\mathrm{rad}} = \sigma \rho \chi T_e^4 \tag{4}$$

where χ is the mean opacity, that is, the cross section per unit mass. Consequently, the radiation mean free path is given by $(\rho\chi)^{-1}$. To assess the relative magnitudes of radiation cooling for the two propellants, mean opacity values for representative plasma parameters of 0.3 gm/m^3 and 3 eV (Fig. 12) were obtained from the SESAME tables [7]. The SESAME model uses spectroscopic data and theory to provide the values for the mean opacities. For the relevant elements the mean opacities are $\chi_{\mathrm{He}} = 408.5$ m^2/kg, $\chi_{\mathrm{N}} = 17.18$ m^2/kg, and $\chi_{\mathrm{H}} = 807.4$ m^2/kg. For commensurate temperature and density values, radiation cooling scales with mean opacity. Because no opacity values for the ammonia plasma mixture are available we can formulate a mass-averaged opacity, $\bar{\chi}_{\mathrm{NH3}} = (14\chi_{\mathrm{N}} + 3\chi_{\mathrm{H}})/17 = 156.6$ m^2/kg which is compared to $\chi_{\mathrm{He}} = 408.5$ m^2/kg to show that radiation cooling effects can be reasonably expected to be diminished.

Conclusions

The time-dependent, two-dimensional, axisymmetric magnetohydrodynamic code MACH2 was upgraded to include an ammonia thermodynamic model and used to simulate the performance of the pulsed inductive thruster operation with ammonia propellant. The computed results were compared to magnetic field waveforms obtained from magnetic probe measurements at two different locations and to total impulse data for a wide range of operating conditions. The code's predictions of the oscillatory waveform agreed well with the first half-period of the pulsed discharge capturing rise time and magnitude of the magnetic field at both locations. The circuit used to model energy deposition was limited to constant resistance and inductance, thus current-reversal time and absolute minimum current values were underestimated. However, the associated acceleration from the second half-period is substantially reduced when compared to that of the first half-period; thus the computed total impulse value underestimated experimental measurements by only 10%. This secondary acceleration is even further reduced when operating at lower stored energy levels, so comparisons of total impulse to experiment in the range of 900–2304 J and variable propellant mass values of 1.9–3.8 mg produced good agreement. Both experiment and modeling in this energy range show that operation with ammonia produces higher efficiency than other propellants such as helium and argon with efficiency increasing as a function of specific operating energy. It is hypothesized that the main factor for ammonia's superior performance over other propellants is its substantially diminished energy transfer by radiation. Furthermore, interrogation of plasma flow characteristics calculated by MACH2 demonstrate strong coupling of the magnetic field with a portion of the propellant which is efficiently accelerated. The remaining gas is entrained in an initial snowplow fashion persisting for the first half-period of the current waveform. The plasma continues to accelerate with some contribution from the second half-period of the oscillatory magnetic field as well as contributions from enthalpy conversion downstream of the confining region.

References

[1] Dailey, L. C., and Lovberg, R. H., "The PIT MkV Pulsed Inductive Thruster," NASA, Contractor Rept. 191155, July 1993.

[2] Peterkin, R. E., Jr., and Frese, M. H., "MACH: A Reference Manual," 1st ed., Air Force Research Laboratory, Phillips Research Site, 10 July 1998.

[3] Mikellides, P. G., and Neilly, C., "Pulsed Inductive Thruster, Part 1: Modeling, Validation and Performance Analysis," AIAA Paper 2004-4091, 2004.

[4] Frese, M. H., "MACH2: A Two-Dimensional Magnetohydrodynamics Simulation Code for Complex Experimental Configurations," Mission Research Corporation, AMRC-R-874, Los Alamos, NM, Sept. 1986.

[5] Braginskii, S. I., "Transport Processes in a Plasma," *Review of Plasma Physics*, edited by M. A. Leontovich, Consultants Bureau, New York, 1965.

[6] Degnan, J. H., and Peterkin, R. E., Jr., "Compact Toroid Formation, Compression, and Acceleration," *Physics of Fluids B*, Vol. 5, No. 8, 1993, pp. 2938–2945.

[7] Holian, K. S., "T-4 Handbook of Material Properties Data Base. Vol Ic: EOS," Los Alamos National Laboratory, LA-1160-MS, Los Alamos, NM, Nov. 1984.

[8] Allison, D. L., and Mikellides, P. G., "A High-Temperature, Thermal Non-Equilibrium Equation of State for Ammonia," *International Journal of Thermophysics*, April 2006, pp. 1–26, http://dx.doi.org/10.1007/s10765-006-0065-y.

[9] Mikellides, P. G., "Numerical Simulations of the Pulsed Inductive Thruster," *Space Technology and Applications International Forum Proceedings*, ISBN 0-7354-0115-2, Vol. 654, STAIF, Albuquerque, NM, 2003, pp. 540–546.